Exp Fluids (2013) 54:1477
DOI 10.1007/s00348-013-1477-7

RESEARCH ARTICLE

A temporal proper decomposition (TPOD) for closed-loop flow control

Stanislav V. Gordeyev · Flint O. Thomas

Received: 22 April 2012 / Revised: 30 January 2013 / Accepted: 5 February 2013

Abstract Motivated by closed-loop flow control applications, a formulation of the proper orthogonal decomposition (POD) is demonstrated, which is capable of characterizing not only the controlled and natural states of a given flow, but also the transient behavior between these states. This approach, which is termed temporal POD (TPOD), extracts the optimum frame of reference and the temporal information regarding the dynamics of the flow in the natural, controlled and transient states. In this paper, the TPOD concept is developed and is subsequently demonstrated in two experiments using dielectric barrier discharge plasma flow control: (1) flow over a circular cylinder at subcritical Reynolds number and (2) flow over a NACA 0015 airfoil at a large post-stall angle of attack. Both flows exhibit well-defined and distinct natural and controlled flow states. For the cylinder flow, the TPOD technique is used to develop a low-order dynamical systems model that is shown to properly capture the dynamics of the first TPOD mode, including the natural, forced and transient regimes. In the airfoil experiment, the TPOD approach is shown to provide the unique ability to conditionally examine the families of flow trajectories between natural and controlled states for user-selected initial conditions. This can be extremely useful in order to understand the physical mechanisms of flow control in complex flows where there may be very little a priori knowledge regarding the system behavior.

This article is part of the collection Topics in Flow Control. Guest Editors J. P. Bonnet and L. Cattafesta.

S. V. Gordeyev · F. O. Thomas (✉)
Department of Aerospace and Mechanical Engineering,
Institute for Flow Physics and Control, University of Notre Dame,
Notre Dame, IN 46556, USA
e-mail: Flint.O.Thomas.1@nd.edu

1 Introduction and motivation

For application to closed-loop flow control, it is desirable to obtain a low-order model of the candidate flow field that satisfactorily captures the dynamics of both the natural and controlled states, as well as transient regimes between these states. It is well known that conventional proper orthogonal decomposition (POD)-based modeling extracts an optimal, complete set of dominant (in terms of energy) spatial modes, such that a minimum number of modes are required to represent a particular flow state (e.g., Berkooz et al. 1993; Holmes et al. 1996; Lumley 1970). The projection of these modes onto the governing Navier–Stokes (N–S) equations provides a low-dimensional system of ordinary differential equations that describes the temporal evolution of the modes as demonstrated in Aubry et al. (1988) and Ukeiley et al. (2001). It is clear that this approach can suffer if the flow field is manipulated by some form of flow control, such that the natural and controlled states of the flow become sufficiently dissimilar. When flow control is activated, the set of POD modes derived to describe the natural flow with as few eigenvectors as possible can become quite nonoptimal for the controlled flow. Consequently, although the set of POD modes is still complete, there is a dramatic increase in the number of POD modes needed to provide a proper frame of reference to describe the forced flow. This is not satisfactory for closed-loop flow control applications. This problem has long been recognized and several modifications of the basic POD approach have been proposed to address this issue. For periodic flows, the so-called double POD or DPOD (Siegel et al. 2008a, b) provides a set of POD modes calculated within each period, and then a second POD-optimization among POD modes is performed between periods, thus providing the eigenvector basis to optimally describe the natural, the transient and the forced states. However, the method may not be readily extended to

Published online: 03 March 2013

more general aperiodic flows. Split POD (Camphouse et al. 2008) provides an extended POD basis which is optimal for both the natural and the forced states, but may not be optimal for the transient state, thus potentially losing information regarding how the flow goes from the natural to the forced state and back. Balanced POD was demonstrated by Rowley (2005) to capture proper dynamical modes from the flow, but can be used only in computational studies, since it requires the solution of the adjoint problem. A technique called the eigensystem realization algorithm (Juang and Pappa 1985) has recently shown some promise to calculate the balanced POD modes directly from experiments as described by Ma et al. (2010).

All of the aforementioned techniques extract an optimal set of spatial eigenmodes to describe the system evolution under the influence of flow control. However, to extract the temporal evolution or trajectories of these modes, they rely on either the Galerkin projection into the N–S equations or an empirical set of temporal equations. The former approach usually suffers from the closure problem, while the second requires a significant amount of empirical knowledge about the underlying system dynamics.

In this paper, an alternative to the approaches outlined above is presented; a new time-dependent version of the POD procedure is described in the following section. The method is quite general and is suitable for application to aperiodic flows. No prior assumptions are made regarding the nature of the flow field dynamics. For the sake of clarity, we describe a two-dimensional version of the method, with a straightforward extension to a three-dimensional version. To demonstrate the effectiveness of the proposed temporal POD (TPOD) technique, the flow behind the circular cylinder at a moderate subcritical Reynolds number was chosen. This flow has well-understood vortex-street dynamics (e.g., Zdravkovich 1997) and has been extensively studied using different low-dimensional techniques (see Siegel et al. (2008a, b) and references therein). In Sect. 3, the experimental apparatus, the principle of operation of the plasma actuator as a flow control device and the velocity field extraction procedure are described. In Sect. 4, we apply the TPOD technique to the experimental realizations of the instantaneous velocity field downstream of the cylinder both with and without flow control to extract the dominant TPOD mode. A simple nonlinear model is developed in Sect. 5 to correctly predict its dynamical evolution. Conclusions and a closing discussion are provided in Sect. 6.

2 Time-dependent POD approach (TPOD)

Consider a system which at any moment, t, is described by an instantaneous field or a trajectory, $u(x, y, t)_\alpha$, where α denotes a particular realization. The flow control is activated at time $t = t_0$, so the system is in the natural state $u^N(x, y, t)_\alpha$ for $t < t_0$ and is in the forced or controlled state $u^C(x, y, t)_\alpha$ for $t - t_0 \to \infty$. The traditional low-dimensional POD approach consists of computing eigenvectors $\{\phi_i(x, y)\}$ for any stationary state as solutions of the eigenvalue problem,

$$\int R_{\beta\gamma}(x, y; x', y')\phi_\gamma(x', y')\mathrm{d}x'\mathrm{d}y' = \lambda\phi_\beta(x, y), \tag{1}$$

where $R_{\beta\gamma}(x, y; x', y') = \overline{u(x, y, t)u(x', y', t)}$ is a cross-correlation matrix, eigenvalue λ_i gives the average energy of each mode, and the overbar denotes averaging in the time-domain. The system is then typically approximated by a (relatively) small number of modes, $u(x, y; t) \approx \sum_i^N a_i(t)\phi_i(x, y)$. After projecting the truncated set onto the N–S equations, the system of ODEs for the temporal coefficients, $a_i(t)$, can be derived as:

$$\frac{\mathrm{d}a_i(t)}{\mathrm{d}t} = Aa_i(t) + Q(a, a) + N(a) \tag{2}$$

where A, Q and N are constant matrices, responsible for linear mode evolution (convection, production and dissipation), quadratic interaction between modes (energy transfer) and nonlinear stabilizing terms, respectively.

Both the natural and controlled states are stationary states, so they can be described by *separate* sets of POD modes, $\{\phi_i^N(x, y)\}$ and $\{\phi_i^C(x, y)\}$, respectively. These sets describe the system in both states, as implemented in split POD (Camphouse et al. 2008), but the very important information about *how the system gets from the natural to the controlled state* is completely lost during time-averaging. So, in order to extract information regarding the trajectory during the transient regime, another averaging operator is needed.

Note that by activating the flow control at time $t = t_0$, the system becomes nonstationary, and therefore, it can be written as a function of time delay after the flow control is activated, $\tau = t - t_0$, as $u(x, y, \tau = t - t_0; t_0 \in \{t_0\}_\alpha)$, where t_0 defines an instant when this trajectory starts; that is, it provides *the initial condition* of the trajectory. Thus, the full set of trajectories describes the system response to the actuation as a function of both the time delay and the initial condition; that is, the state of the flow when the control was first applied.

Depending on the initial condition, the system response to the same actuation might be different. To quantify this, let us consider a subset of trajectories originating from a small region of initial conditions centered at a fixed moment T_0, $t_0 \in \{t_0\}(\varepsilon, T_0) : |u(u, y, \tau = 0; t_0) - u(x, y, \tau, T_0)| \le \varepsilon$, as shown schematically in Fig. 1. For every fixed time delay, let us compute a set of POD modes by cross-correlating system trajectories over the subset of trajectories,

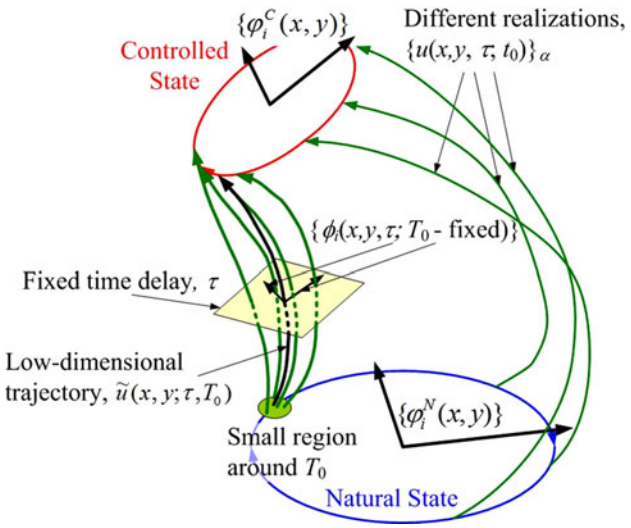

Fig. 1 Topological definition of spatial TPOD modes

$$\int R(x,y,x';y';\tau,T_0)\phi_i(x',y';\tau,T_0)\mathrm{d}x'\mathrm{d}y' = \lambda_i(\tau,T_0)\phi_i(x,y,\tau,T_0), \quad \|\phi_i\|^2 = 1, \tag{3}$$

where $R(x,y;x',y';\tau,T_0) = E\{u(x,y;\tau,t_0)\cdot u(x',y';\tau,T_0)\}_{\{t_0\}(\varepsilon,T_0)}$. Each flow trajectory in the subset can be represented in the low-dimensional space spanned by *spatio-temporal* eigenmodes or temporal POD (TPOD) modes as,

$$u(x,y;\tau,t_0\in\{t_0\}(\varepsilon,T_0)) = \sum_i b_i(\tau,t_0)\phi_i(x,y;\tau,T_0), \tag{4a}$$

and each temporal coefficient is calculated by projecting the instantaneous flow trajectory into a TPOD mode,

$$b_i(\tau;t_0) = \int u(x,y;\tau,t_0\in\{t_0\}(\varepsilon,T_0))\phi_i(x,y;\tau,T_0)\mathrm{d}x\,\mathrm{d}y \tag{4b}$$

Finally, $E\{b_i^2(\tau,T_0)\}_{\{t_0\}(\varepsilon,T_0)} = \lambda_i(\tau,T_0)$ is the subset-averaged mode energy at a given time delay τ. Thus, based on this definition, the temporal POD decomposes the system trajectories into a series of low-dimensional sets of *spatio-temporal* orthogonal-in-space eigenmodes, $\{\phi_i(x,y,t,T_0)\}$.

Next, we will perform averaging over all trajectories in the subset keeping the time delay fixed to find an averaged trajectory, $\tilde{u}(x,y;\tau,T_0)$, originating from T_0,

$$\begin{aligned}\tilde{u}(x,y;\tau,T_0) &= E\{u(x,y;\tau,T_0)\}_{\{t_0(\varepsilon,T_0)\}}\\ &= \sum_i E\{b_i(\tau,t_0)\}_{\{t_0(\varepsilon,T_0)\}}\phi_i(x,y;\tau,T_0)\\ &\equiv \sum_i B_i(\tau,T_0)\phi_i(x,y,\tau,T_0)\end{aligned} \tag{5}$$

Averaging over all trajectories allows one to reduce stochastic, small-scale noise and calculate a finite set of deterministic conditionally averaged trajectories $\tilde{u}(x,y;\tau,T_0)$, which describes the large-scale system response to the actuation.

It is convenient to further project each deterministic spatial–temporal TPOD mode, $\phi_i(x,y,\tau,T_0)$, into a set of *spatial* modes, $\psi_{i,j}(x,y)$, using the traditional POD technique as:

$$\phi_i(x,y;\tau,T_0) = \sum_j C_{i,j}(\tau,T_0)\psi_{i,j}(x,y), \quad \|\psi_{i,j}\|^2 = 1, \tag{6}$$

The set of TPOD ψ-modes, after a proper re-orthogonalization, provides the optimal set of spatial eigenvectors to describe the natural, transient and control states. They can be used to expand each individual trajectory as:

$$u(x,y;\tau,t_0) = \sum_{i,j} d_{i,j}(\tau,t_0)\psi_{i,j}(x,y), \tag{7a}$$

or, the set of conditionally averaged trajectories as:

$$\begin{aligned}\tilde{u}(x,y;\tau,T_0) &= \sum_{i,j} B_i(\tau,T_0)\,c_{i,j}(\tau,T_0)\,\psi_{i,j}(x,y)\\ &= \sum_{i,j} a_{i,j}(\tau,T_0)\,\psi_{i,j}(x,y)\end{aligned} \tag{7b}$$

The temporal coefficients, $a_{i,j}(\tau,T_0)$, define conditionally averaged trajectories of the system in the ψ-mode space and can be recovered from $d_{i,j}(\tau,t_0)$ as $a_{i,j}(\tau,T_0) = E\{d_{i,j}(\tau,t_0)\}_{\{t_0\}(\varepsilon,T_0)}$. By construction, as a limit of $\varepsilon\to 0$, $T_0\to t_0$ and $a_{i,j}(\tau,T_0)\to d_{i,j}(\tau,t_0)$.

Another useful property of the ψ-mode space is that it provides an optimal way to store spatial–temporal information about the system. Due to the POD optimal convergence property, only a relatively few ψ-modes and corresponding temporal coefficients, $a_{i,j}(\tau,T_0)$ and/or $d_{i,j}(\tau,\tau_0)$, are needed to faithfully reconstruct the system response from Eqs. (7a) or (7b).

It is worth noting that from Eq. (7a), it follows that ψ-modes can be calculated directly from the original velocity field, u, by applying a traditional POD technique, Eq.(1); however, the temporal evolution of the system, $a_{i,j}(\tau,T_0)$ or $d_{i,j}(\tau,t_0)$, will be lost in the time-averaging procedure.

By construction, TPOD modes, either ϕ- or ψ-modes, provide very important information about *how* the system travels from the natural to the controlled state. The low-dimensional representation of both the natural and controlled states can be recovered from ψ-modes by substituting Eq. (7a) into Eq. (1) as a weighted linear combination of ψ-modes, as $\varphi_i^N(x,y) = \sum_j\left(\overline{d_{i,j}^2(\tau\le 0,t_0)}\right)^{1/2}\psi_{i,j}(x,y)$ and $\varphi_i^C(x,y) = \sum_j\left(\overline{d_{i,j}^2(\tau\to\infty,t_0)}\right)^{1/2}\psi_{i,j}(x,y)$, respectively. A schematic of the TPOD reconstruction of system

trajectories is shown in Fig. 1. For simplicity, both the natural and controlled states are graphically represented by limit cycles. Only a single controlled state is shown in Fig. 1 although multiple controlled states may well exist in a given application. The single control state shown does not represent an assumption inherent to the technique; rather, it is simply a consequence of the set of initial conditions T_0 being sufficiently small to drive the system trajectories to the indicated control state. As indicated, when the flow control is applied at $\tau = 0$, the flow leaves the natural state and approaches the controlled state. Individual trajectories depend on the time delay and the initial time, or the point where the trajectory departs the natural state. All initial times can be described by projecting the trajectories into ψ-modes in the natural state, $u(x, y; \tau = 0, t_0) = \sum_{i,j} d_{i,j}(t_0)\psi_{i,j}(x, y)$. So, each initial time can be represented by the set of temporal coefficients, $\{d_{i,j}(t_0)\}_\alpha$, or in the case of the conditionally averaged set of trajectories, $\tilde{u}(x, y; \tau, T_0)$, by $\{a_{i,j}(T_0)\}_\alpha$. In this manner, the topology of flow trajectories, either original or conditionally averaged, can be analyzed as a function of the initial time and the time delay.

By selecting different initial conditions, the TPOD approach allows one to analyze the temporal response of the system to the flow control. Initial conditions, $\{a_{i,j}(T_0)\}_\alpha$, can be selected either by conditionally sampling data during the experiment or during post-process analysis by selecting different initial regions and performing the averaging, defined in Eq. (7b). Both approaches are demonstrated in this paper. It is shown that the TPOD requires no prior knowledge of the system and provides an optimum eigenspace to study the system's response to the actuation.

For closed-loop flow control applications, it is often desired to develop a low-dimensional model of the system, which correctly describes natural, transient and controlled states. As mentioned before, the original system is governed by the N–S equations, and Galerkin projection of the set of standard POD modes onto the N–S equations gives a system of ODE's to describe the temporal evolution of coefficients for each mode. In general, this system (2) has linear, quadratic and higher-order nonlinear terms. The inclusion of quadratic terms models the nonlinear energy transfer between different resolved turbulent structures or modes, while cubic terms are needed to stabilize the truncated system and model unresolved modes (Ukeiley et al. 2001). Several approaches have been proposed to develop stable models. The artificial neural network (ANN-ARX) and the DPOD approaches (Siegel et al. 2008a, b) were used to develop a stable system of equations to describe the wake evolution behind a cylinder flow in the presence of forcing. Other researchers have looked for a set of equations of specific form, inspired by dynamical systems (e.g., Luchtenburg et al. 2009; Tadmor et al. 2004). A similar, but more general approach, used by Ausseur and Pinier (2005), postulated the presence of linear, quadratic and cubic terms in (2) and found corresponding matrices and tensors using time-dependent POD coefficients extracted from the experiment via the least-square analysis.

Adapting the approach from Ausseur and Pinier (2005), we also seek the temporal evolution of TPOD ψ-modes as a combination of the linear, quadratic and cubic terms,

$$\frac{\mathrm{d}\vec{a}(\tau)}{\mathrm{d}\tau} = A\vec{a}(\tau) + Q\vec{a}(\tau)\vec{a}(\tau) + T\vec{a}(\tau)\vec{a}(\tau)\vec{a}(\tau) + Bf, \qquad (8)$$

where A, Q, T and B are assumed to be constant matrices and tensors. The effect of the actuator forcing "strength," f, is modeled by the linear term Bf, similar to Luchtenburg et al. (2009), Tadmor et al. (2004) and Ausseur and Pinier (2005). Since the temporal evolution of each TPOD mode is known from (7b), the system (8) can be solved to find A, Q, T and B using a least-squares analysis,

$$\sum_{T_0} \int_\tau \left[\frac{\mathrm{d}\vec{a}(\tau, T_0)}{\mathrm{d}\tau} - (A\vec{a} + Q\vec{a}\vec{a} + T\vec{a}\vec{a}\vec{a} + Bf) \right]^2 \mathrm{d}\tau \rightarrow min \qquad (9)$$

and now, the original system is modeled by the set of ODE's (8) with the initial conditions $\{a_{i,j}(\tau = 0, T_0)\}_\alpha$.

We will illustrate the TPOD technique described in this section by applying active control to the flow over a circular cylinder with the natural state, a simple limit cycle suitable to a phase-locking technique. The following section describes the experimental apparatus and the candidate flow field used to demonstrate the TPOD technique. Section 4 presents experimentally extracted TPOD modes for the cylinder flow using conditional sampling in conjunction with conventional particle image velocimetry (PIV). The corresponding modeling results are presented in Sect. 5. In Sect. 6, we briefly present and discuss the experimental results from applying the TPOD to leading edge flow control on a NACA 0015 airfoil.

3 Experimental facility

In order to experimentally demonstrate the TPOD approach, active control of the flow over a circular cylinder in cross-flow using surface-mounted dielectric barrier discharge (DBD) plasma actuators (as described in the optimization study by Thomas et al. 2009) is used. The reader unfamiliar with the application of DBD plasma actuators for active flow control is referred to recent reviews on the subject (e.g., Corke et al. 2009; Moreau 2007). Effective control of circular cylinders in cross-flow using DBD

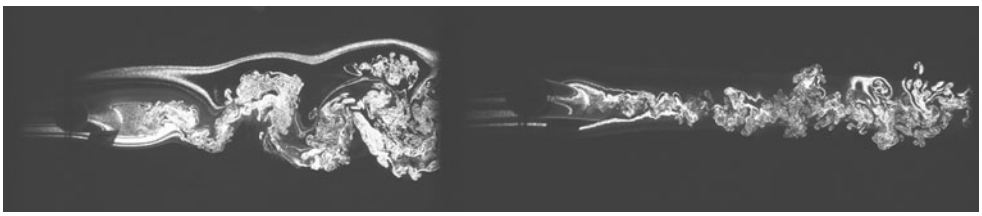

Fig. 2 Visualization of the flow over the circular cylinder at $Re_D = 5{,}000$: (*left*) the natural state (plasma off), (*right*) the controlled state (plasma on)

plasma actuation has been demonstrated in previous experimental studies (Thomas et al. 2008; Kozlov and Thomas 2011). Plasma actuators have been shown to have a dramatic effect on the cylinder wake flow with the complete elimination of unsteady Karman shedding. Consequently, the flow has two very distinct states: the natural state, which features unsteady Karman shedding of large-scale vortices into the wake, and the controlled state, where the separation region is greatly reduced in size and shedding is suppressed. These two states are clearly illustrated in the sample flow visualization images shown in Fig. 2. The flow visualization was obtained by seeding the flow with 1-micron-diameter olive oil droplets which are illuminated by a pulsed Nd-Yag laser sheet in the spanwise centerplane. It should be noted that the focus of this paper is *not* on bluff body plasma flow control. Rather, DBD plasma was utilized simply because it is capable of providing very distinct natural and controlled states with transient system trajectories between these states.

The flow control experiments were performed in one of the low-turbulence, subsonic, in-draft wind tunnels located at the Hessert Laboratory for Aerospace Research at the University of Notre Dame. The wind tunnel has an inlet contraction ratio of 20:1. A series of 12 turbulence management screens at the front of the inlet give rise to tunnel freestream turbulence levels less than 0.1 % (0.06 % for frequencies above 10 Hz). Experiments are performed in a test section of 0.610 m square cross-section and 1.82 m in length. One sidewall and the test section ceiling have optical access for nonintrusive laser flow field diagnostics (in this case PIV).

The cylinder model with twin dielectric barrier discharge (DBD) plasma actuators is shown schematically in Fig. 3. It consists of two coaxial fused quartz tubes: 13.5 mm I.D. × 19 mm O.D. × 533.4 mm long and 6 mm I.D. × 13 mm O.D. × 533.4 mm long. The outer cylinder wall (1) serves as the dielectric barrier for the DBD actuators; the dielectric constant of quartz is 3.7. The overall cylinder O.D. was $D = 19$ mm. The ends of the cylinder terminate in plastic endplates, which elongate the model by 19.05 mm. Tunnel blockage due to the cylinder model was only 2.7 % and no blockage corrections were applied to the experimental results. The exposed and insulated electrodes

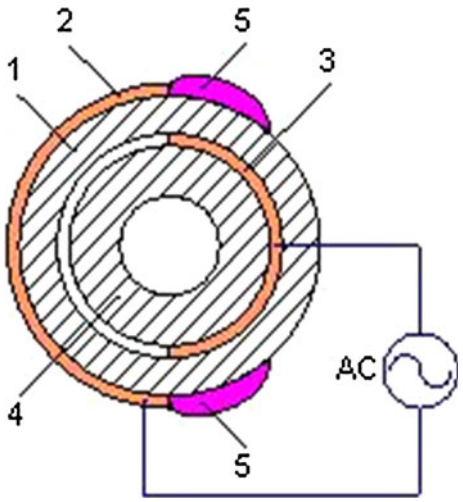

Fig. 3 Schematic of the cylinder model

are common for both of the plasma actuators due to space limitations. These electrodes are made of Saint Gobain C661 1.6 mil (0.041 mm)-thick copper foil tape with acrylic adhesive. As indicated, the outer, exposed electrode (2) is mounted to the surface of the outer quartz tube with its plasma generating edges located at ±90° with respect to the approach flow direction (left-to-right in Fig. 3). The insulated electrode (3) is mounted to the outer surface of the inner quartz tube (4). Both inner and outer electrodes extend 444.5 mm in the spanwise direction (approximately 84 % of the cylinder model span). The inner and outer electrodes have a small overlap, which gives rise to a large local electric field. Plasma (5) forms near the edge of the exposed electrode and extends a distance along the cylinder's dielectric surface as depicted in Fig. 3. As indicated in the figure, the actuators are connected to a high voltage ac source that provides 62 kV peak-to-peak positive ramp waveform excitation to the electrodes at a frequency of 1 kHz. The high-frequency, high-amplitude ac voltage is created using the circuit described in Kozlov and Thomas (2011). As noted in Thomas et al. (2008), DBD plasma flow control can be applied in either a quasi-steady or unsteady manner. For the work reported in this paper, the plasma actuators on the cylinder were always operated in a quasi-steady mode in the sense that an unmodulated

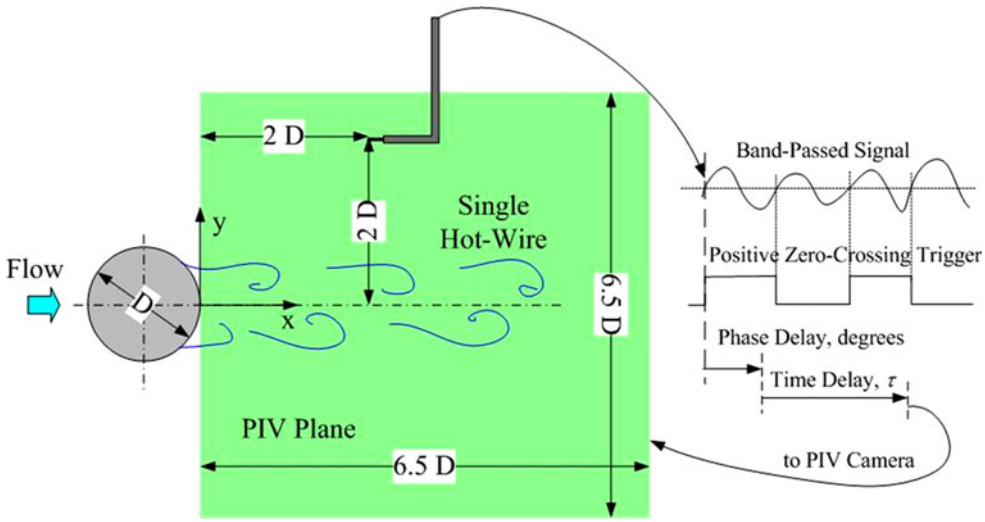

Fig. 4 Schematic of experimental setup with hot-wire signal as a trigger

ac carrier of 1 kHz constant frequency was used when flow control was applied. The time-scale for vortex shedding is two orders of magnitude larger than that associated with plasma formation. In this manner, flow control occurs by way of quasi-steady, plasma-induced tangential wall jets, which in conjunction with a Coanda effect significantly delay boundary layer separation from the cylinder surface.

The velocity field data for the TPOD analysis were obtained nonintrusively by using PIV measurements. The air upstream of the wind tunnel inlet was seeded with olive oil droplets of nominally 1-micron diameter that are produced by a TSI atomizer. A model Y120-15 New Wave Research Nd:Yag laser produced double laser pulses with a 25-μs time interval. The maximum pulse repetition rate for this laser was 15 Hz. PIV images were captured by a PIV CAM 10-30 digital camera. TSI Insight 6 software was used to obtain a vector velocity field from each image pair. The interrogation region was approximately 6.5 cylinder diameters downstream of the end of the cylinder and 6.5 diameters in the cross-stream direction as shown schematically in Fig. 4.

The free stream velocity for the experiments was $U_\infty = 4$ m/s, which corresponds to a Reynolds number based on cylinder diameter, D, of approximately $Re_D = 5{,}000$. This certainly does not represent an upper Reynolds number limit for effective bluff body plasma flow control (see Kozlov and Thomas 2011). Rather, it was deemed sufficient for demonstrating the TPOD technique. The corresponding Strouhal number associated with Karman vortex shedding was $St_D = 0.2$ in good agreement with published values at comparable Reynolds number. The experiment consisted of multiple cycles of turning the twin DBD plasma actuators on and off. As implied by Fig. 3, the twin plasma actuators were always operated in phase. Turning the plasma actuators on took the flow from the natural to controlled state and subsequently turning the plasma off allowed the flow to return to the natural state. In the experiments, the plasma was turned on for 125 ms and then turned off for 235 ms, so that the corresponding single plasma on–off cycle period was 360 ms. The plasma on–off cycle was nonintrusively sampled via PIV with variable delay time steps (to be described later), referenced from the moment the plasma actuators were turned on (time $= t_0$ as shown in Fig. 1). The resulting PIV data set was conditionally sampled to obtain 300 independent realizations for each fixed value of the time delay, τ, relative to plasma initiation. This number of independent ensembles was found sufficient for statistical convergence.

In order to distinguish between different paths from the natural to the controlled state, the TPOD approach should be applied for different small regions of initial times, $u(x, y, \tau; t_0 \in \{t_0\}(\varepsilon, T_0))$. In the case of a flow with natural time-periodic motion like the one under consideration here, it is desirable to phase lock the initiation of plasma flow control relative to the flow's natural state (e.g., with respect to a particular phase of the cylinder's natural shedding cycle). In doing this, one phase locks the trajectory in phase space that takes the flow from the natural to controlled state. In order to fix t_0 relative to the natural shedding cycle, a single constant temperature hot-wire probe was placed at $x = 2D$ downstream of the cylinder trailing edge, $y = 2D$ above the cylinder axis and $z = 0.4D$ spanwise offset between the probe and the PIV laser light sheet, as shown schematically in Fig. 4. Although the hot-wire probe was outside the cylinder wake, it sensed the wake shedding state via Biot–Savart induction from the large-scale wake vortices. The hot-wire velocity signal was filtered in a narrow band centered on the Strouhal shedding frequency of $f = 42$ Hz and was ac-coupled. A phase reference point was assigned to the hot-wire signal-positive zero-crossing event with a voltage comparator circuit (see Fig. 4). A fixed phase delay was added to the phase reference point to define the phase-

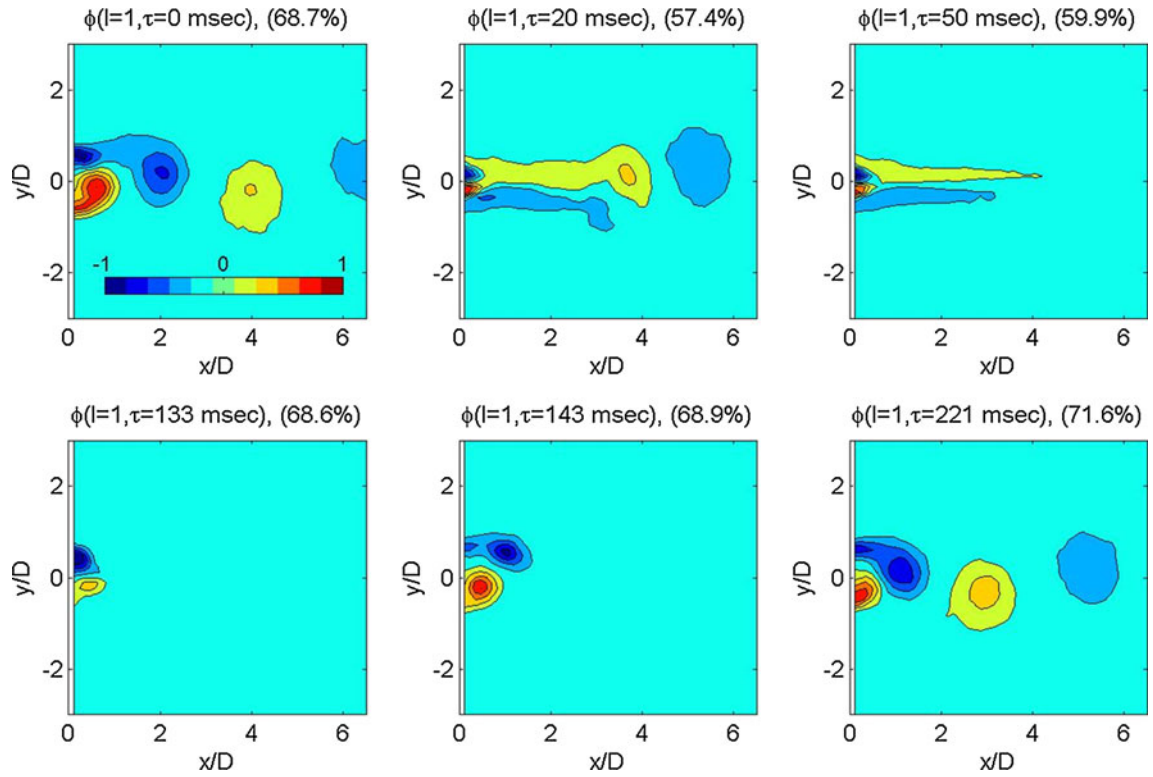

Fig. 5 The spanwise-component vorticity associated with the first TPOD mode, $\phi_1(x, y; \tau)$ at different representative time delays, τ. The actuation is turned on at $\tau = 0$ ms and is turned off at $\tau = 125$ ms. Phase shift t_0 is defined as 0° with respect to the natural shedding cycle. *Numbers* in *parenthesis* are the relative amounts of energy in TPOD mode 1; $\lambda_1(\tau)/\sum_i \lambda_i(\tau)$

locked state (i.e., to specify t_0), and the PIV camera was triggered after a given time delay from this phase delay, as shown in Fig. 4. In this manner, multiple flow field realizations could be acquired for plasma initiated at a selected phase (t_0) of the natural shedding cycle and at the desired time delay, τ, relative to plasma initiation.

4 Experimental results

In this section, representative experimental results are presented which serve to illustrate application of the TPOD for flow field characterization during transient flow control.

The experimental 2D velocity field was processed to extract time-dependent TPOD modes using the method of snapshots (Sirovich 1987). The freestream velocity was subtracted from each resulting velocity field. The TPOD was performed on the velocity field and the eigenvalues have units of kinetic energy. However, for convenience, all POD modes in this paper will be presented in terms of spanwise vorticity. Figure 5 shows the spanwise vorticity associated with the first TPOD mode at several representative time delays, τ, from both the actuation on and off parts of the cycle. For this figure, actuation initiation time t_0 corresponds

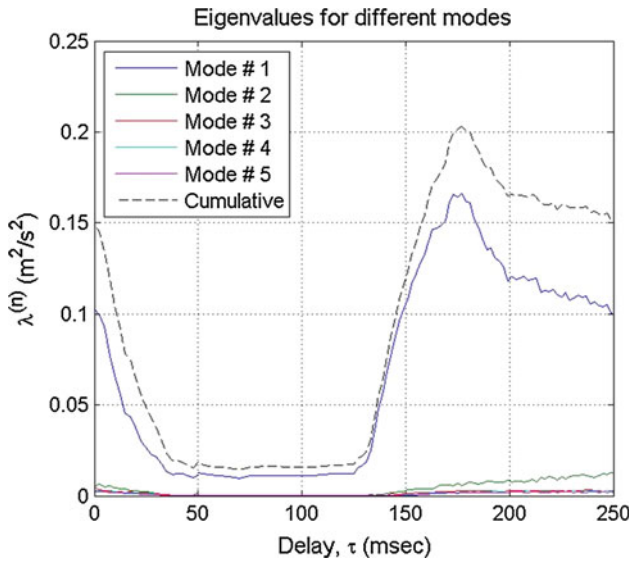

Fig. 6 TPOD mode 1…5 eigenvalues, $\lambda_i(\tau)$ and cumulative energy $\sum_i \lambda_i(\tau)$

to the zero-degree (arbitrarily defined) phase angle with respect to the natural shedding cycle. The corresponding temporal evolution of energy (i.e., eigenvalues) for the first 5 TPOD modes is shown in Fig. 6. It was found that the first TPOD mode holds approximately 60–85 % of the total

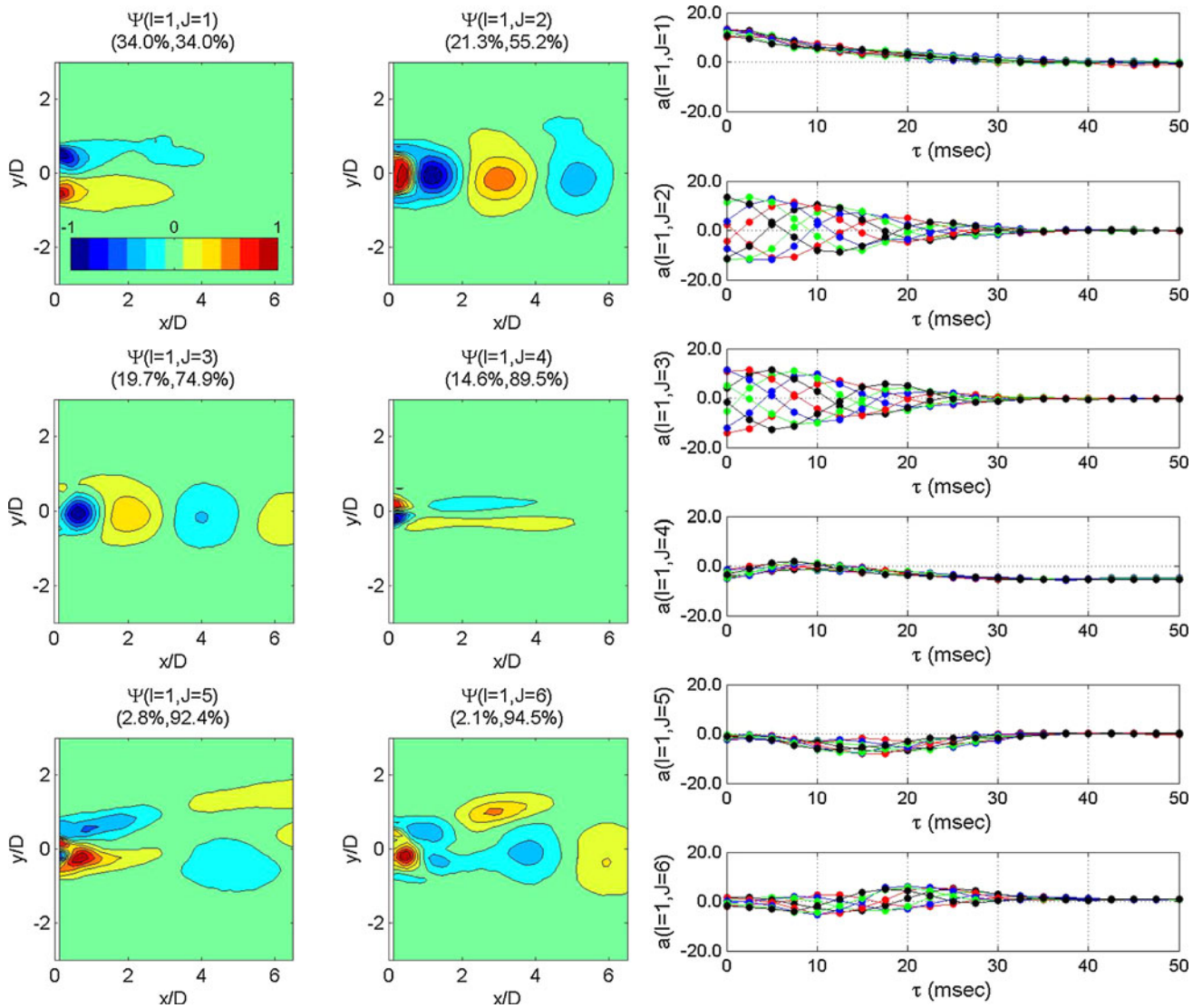

Fig. 7 (*Left*) modes $\psi(1, j)$ and (*right*) corresponding temporal coefficients $a(1, j)$, defined in Eq. (7b) for eight different phases for $\tau = 0 \ldots 50$ ms. Flow control was turned on at $\tau = 0$ ms

resolved kinetic energy depending on the time delay, τ. Values at several representative time delays are shown in parentheses in Fig. 5. It is apparent from examination of both Figs. 5 and 6 that the flow undergoes a rather drastic change as it switches from the natural to the controlled state. This occurs between time delays of $\tau = 0$ and approximately 50 ms as vortex shedding is eliminated. The plasma flow control is terminated at $\tau = 125$ ms, and Fig. 5 images at $\tau = 143$ ms and 221 ms, show the renewal of vortex shedding, while Fig. 6 shows a corresponding increase in modal energy content with τ once the plasma is extinguished. Clearly, the flow is phase-locked, so that shed vortices are seen in Fig. 5 at $\tau = 143$ and 221 ms, for instance.

Knowing the TPOD modes at given discrete time delays, τ, the first six spatial-only $\psi_{i,j} = \psi(i, j)$-modes (Eq. 6) for the first TPOD mode, $\phi_1(x, y; \tau)$are presented in Fig. 7, left plots. The first mode, $\psi(1, 1)$, represents the ensemble-averaged natural flow. The fourth mode, $\psi(1, 4)$, is a linear combination of the ensemble-averaged flows during the natural and actuated states and is related to the so-called shift mode described in Siegel et al. (2008a); the second and the third modes, $\psi(1, 2)$ and $\psi(1, 3)$, describe the vortex shedding behind the cylinder and higher modes are responsible for the transient regime between the natural and the controlled cases. It should be emphasized that spatial modes $\psi(1, j)$ shown in Fig. 7 represent an *optimum basis* for describing natural, actuated and transient states of the cylinder flow field.

Corresponding temporal coefficients, $a_{1,j} = a(1, j)$, (Eq. (7b)) for the first six ψ-modes for eight phases, t_0, were

calculated by projecting the first TPOD mode into the spatial ψ-mode frame of reference. These are shown in Fig. 7, right plots. These coefficients represent the temporal evolution of the "most-energetic" portion of the flow from the given phase point on the natural cycle during the time interval associated with transition from natural to controlled state (see Fig. 6). In each case, $a(1, j)$ is shown for eight values of initial phase, t_o, and these are distinguished by color. As expected, the temporal evolution of the second and the third ψ-modes, which are responsible for the shedding cycle, strongly depends on the initial phase, t_0. The phase dependence of the temporal evolution of the first and the forth ψ-modes is negligible, implying that the change in the ensemble-averaged flow does not depend on the phase of the shedding cycle (at least for the particular conditions of this experiment). Finally, the fifth and the sixth ψ-modes, which are responsible for the transient effects, also show a moderate dependence on the initial shedding phase. Note that with the exception of $a(1, 4)$ (the shift mode), all values of $a(1, j)$ approach 0 at the end of the transition from natural to controlled state. This is indicative of the flow reaching a new stationary controlled state.

In order to check how well the velocity realizations were phase-locked at the moment the flow control was turned on, which corresponded to the delay time $\tau = 0$, all individual flow realizations for all phases were projected into the vortex-shedding ψ-modes, $\psi(1, 2)$ and $\psi(1, 3)$. The result is presented in Fig. 8. This figure plots instantaneous values of $d_{1,3}(\tau = 0, t_0)$ versus $d_{1,2}(\tau = 0, t_0)$for each selected value of initial condition t_0 (Eq. 7a). The two phases of 0° and 180° are highlighted by blue and red symbols, respectively. Also, the temporal coefficients of the first TPOD mode, $a(1, 2)$ and $a(1, 3)$, at $\tau = 0$ for each phase are presented as solid black circles in Fig. 8. The system in the natural state clearly exhibits limit cycle behavior in this ψ-mode space. Individual velocity realizations are relatively highly clustered around the corresponding selected phase points, thus verifying the hot-wire-based conditional-sampling technique as well as the inherent stochastic character of individual trajectories between natural and controlled states.

After the flow control is applied, the flow approaches a steady-state which does not exhibit vortex shedding, and it therefore "loses memory" regarding the initial phase the flow was in when the flow control was first applied. Thus, the phase-locking technique used to select the initial flow state, as validated in Fig. 8, will no longer apply when the actuation is turned off, that is, for time delays larger than $\tau = 125$ ms in the current experiment. Figure 9 shows the temporal evolution of the $a_{1,j}$-coefficients (Eq. 7b) during both the natural to control transition when plasma actuation was turned on ($\tau = 0\ldots125$ ms), and during control to natural transition when plasma actuation was turned off, ($\tau = 125\ldots250$ ms). While the phase-locking technique was obviously able to separate different trajectories during the natural to control transition, only one trajectory was extracted during control to natural transition as shown in Fig. 9. When flow control was turned off, the flow started separating on both sides of the cylinder and initially formed a nearly symmetric pair of starting vortices. But shortly after the plasma was extinguished as observed in Fig. 5 for $\tau = 133$ ms, one vortex was always slightly stronger than its counterpart, and this is most likely due to a very small asymmetry of the cylinder model. Due to a mutual vortex interaction, it would shortly thereafter move farther downstream (see Fig. 5 for $\tau = 143$ ms) eventually giving rise to asymmetric vortex shedding, and this would effectively "phase-lock" the flow. Figure 10 presents projections of the instantaneous flow field into the second and third ψ-TPOD modes at different time delays $\{d_{1,2}(\tau), d_{1,3}(\tau)\}$. Note that the instantaneous projections tend to cluster around the ensemble-averaged points $(a_{1,2}, a_{1,3})$defined in Eq. (7b), although not nearly as compact as in Fig. 8. In the absence of any natural "phase-locking," instantaneous

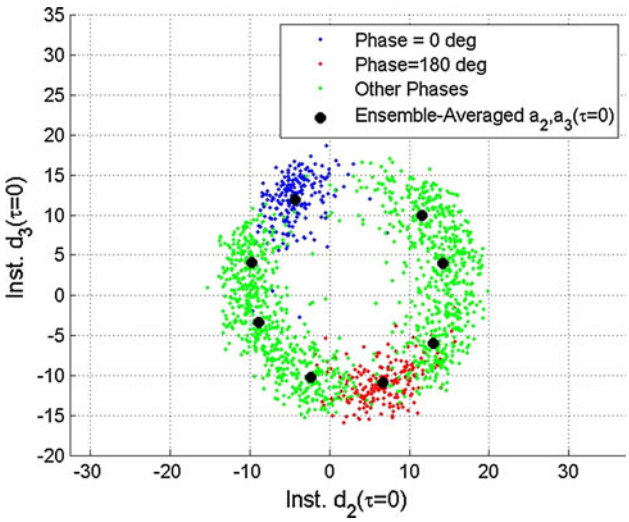

Fig. 8 Projection of instantaneous velocity fields, $\{d_2, d_3\}$, (*dots*), and the dominant ϕ_1-mode, $\{a_2, a_3\}$, (*filled circles*) into $\psi(1, 2)$ and $\psi(1, 3)$, defined in Eqs. (7a) and (7b), respectively, for different phases for $\tau = 0$

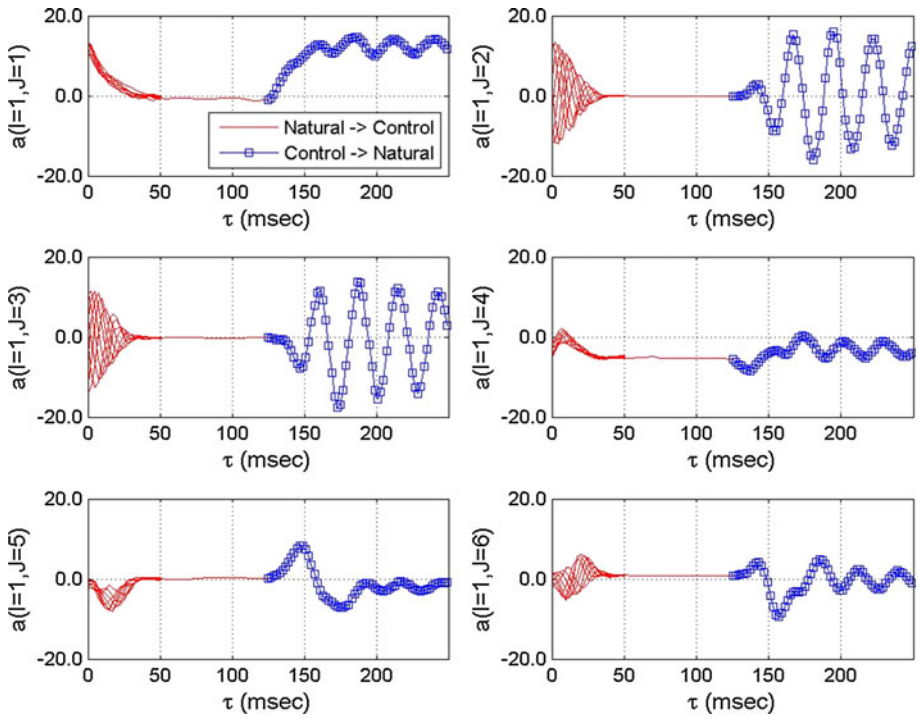

Fig. 9 Temporal coefficients $a(1, j)$, as defined in Eq. (7b) for eight different initial phases for $\tau = 0 \ldots 250$ ms. Flow control was turned on at $\tau = 0$ ms and turned off at $\tau = 125$ ms. *Red* denotes control on and *blue* control off intervals

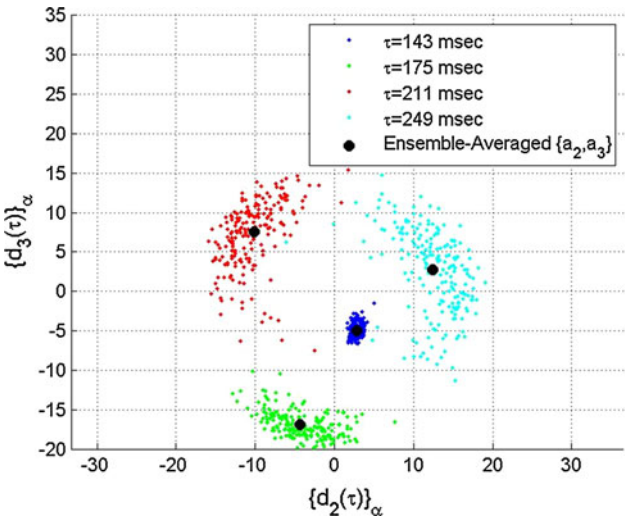

Fig. 10 Projection of instantaneous velocity fields, $\{d_2, d_3\}$, (*dots*), and the dominant ϕ_1-mode $\{a_2, a_3\}$, (*filled circles*) into $\psi(1, 2)$ and $\psi(1, 3)$, defined in Eqs. (7a) and (7b), respectively, for different time delays, $\tau > 125$ ms, when the actuation is turned off

projections would be evenly distributed on the limiting cycle and a-coefficients for the second and the third ψ modes would be zero. Hence, we see that after flow control is turned off, a weaker natural phase lock remains, which is independent of t_0. This will have implications regarding the application of the TPOD results to dynamical system modeling as described in the next section.

5 Modeling

Experimentally extracted coefficients for the dominant ϕ_1-mode at the fixed phase, $a_{1,j}(\tau, t_0 = \text{fixed}) \equiv a_j(\tau)$, Eq. (7b), of the first six ψ-modes were used to calculate matrices in (8). Different combinations of the nonlinear terms, up to cubic terms, as discussed in the Introduction, were tried in order to get the best agreement between the experimental and modeled coefficients, while keeping a minimum number of nonlinear terms. Different combinations of nonlinear terms were tried manually to achieve the best agreement between the experimentally observed and modeled dynamics, as the model should predict experimental behavior not only from a minimal mean-square error point of view but also in resolving the main dynamical features, especially during transient regimes. This manual approach *did not* involve trying all possible combinations of nonlinear terms and required a somewhat subjective judgment. Despite these limitations, the results clearly show the possibility of the TPOD approach to provide a low-dimensional model with a fairly small number of coefficients. In the future, automated algorithms could be used to check all possible combinations of nonlinear terms in order to identify their dynamical importance and whether they should be kept in the model. This approach will allow the system to be properly modeled with the minimum number of terms. Also, studying why specific terms should be kept in the model will give additional information about the inherent dynamics of the system.

After several iterations, the system (8) was finally written as the following system of ODE's:

$$
\begin{aligned}
\frac{da_1(\tau)}{d\tau} &= c_1 + l_{11}a_1 + q_{141}a_4a_1 + q_{111}a_1^2 + q_{121}a_2a_1 \\
&\quad + q_{131}a_3a_1 + b_1f \\
\frac{da_2(\tau)}{d\tau} &= c_2 + \left[l_{22} + t_2\left(a_2^2 + a_3^2\right)\right]a_2 + l_{23}a_3 \\
&\quad + q_{212}a_1a_2 + b_2f \\
\frac{da_3(\tau)}{d\tau} &= c_3 + l_{32}a_2 + \left[l_{33} + t_3\left(a_2^2 + a_3^2\right)\right]a_3 + q_{313}a_1a_3 \\
&\quad + q_{314}a_1a_4 + b_3f \\
\frac{da_4(\tau)}{d\tau} &= c_4 + l_{41}a_1 + l_{44}a_4 + q_{444}a_4^2 + q_{414}a_1a_4 \\
&\quad + q_{424}a_2a_4 + q_{434}a_3a_4 + b_4f \\
\frac{da_5(\tau)}{d\tau} &= c_5 + l_{51}a_1 + \left[l_{55} + t_5\left(a_5^2 + a_6^2\right)\right]a_5 + l_{56}a_6 \\
&\quad + q_{515}a_1a_5 + q_{525}a_2a_5 + q_{535}a_3a_5 + b_5f \\
\frac{da_6(\tau)}{d\tau} &= c_6 + l_{61}a_1 + l_{62}a_2 + l_{63}a_3 + l_{65}a_5 \\
&\quad + \left[l_{66} + t_6\left(a_5^2 + a_6^2\right)\right]a_6 + q_{626}a_2a_6 + q_{636}a_3a_6 \\
&\quad + q_{646}a_4a_6 + q_{656}a_5a_6 + b_6f
\end{aligned} \tag{10}
$$

In order to model the temporal evolution of the first and the fourth (shift) modes responsible for the mean flow evolution in the presence of the forcing, only the linear and quadratic terms were explicitly included. Equations for the vortex-shedding modes, a_2 and a_3, have the simple cubic stabilizing terms, $t_2\left(a_2^2 + a_3^2\right)a_2$ and $t_3\left(a_2^2 + a_3^2\right)a_3$, which ensures that the modes will have stable limit cycles. Interactions with the mean flow, a_1, and the shift mode, a_4, were modeled by including quadratic terms, $q_{212}\,a_1\,a_2$, $q_{313}\,a_1\,a_3$ and $q_{314}\,a_1\,a_4$. Equations for the transient terms, a_5 and a_6, have similar stabilizing cubic terms, $t_5\left(a_5^2 + a_6^2\right)a_5$ and $t_6\left(a_5^2 + a_6^2\right)a_6$, and interactions with the mean flow modes, a_1 and a_4, and the vortex-shedding modes, a_2 and a_3, were modeled using selected quadratic terms. Temporal coefficients were re-interpolated into a uniform time interval with a 1-ms time step, and temporal derivatives at discrete times, $da_j(\tau)/d\tau$, were numerically calculated using the second-order finite difference approximation, $da_j(\tau)/d\tau \approx \left(a_j(t+\Delta\tau) - a_j(t-\Delta\tau)\right)/2\Delta\tau$, with $\Delta\tau = 1$ ms. The least-squares procedure was used to find the best fit for all unknown coefficients. The resulting numerical values are summarized in Table 1.

The system (10) was solved numerically over the time interval [0…250 ms] with a numerical time step of 0.01 ms using the initial conditions of the a-coefficients at $\tau = 0$ for the phase-locking value of zero degrees. The forcing term was $f = 1$ for $\tau = 0\ldots125$ ms and $f = 0$ for $\tau = 125\ldots250$ ms. Results of the modeling along with a comparison with experimental values are presented in Fig. 11. The system of Eq. (10) correctly predicts the essential features of the temporal evolution of the first six TPOD modes. Using values from Table 1, the natural shedding frequency was calculated to be 38 Hz, which is very close to the experimentally observed frequency of approximately 42 Hz. The first and fourth modes, $a_1(\tau)$ and $a_4(\tau)$, correctly predict the mean flow changes with the forcing turned on and off, but exhibited a slightly higher oscillatory behavior when the forcing was switched off. The modeled values of the vortex-shedding modes, $a_3(\tau)$ and $a_4(\tau)$, are in good agreement with the experimental values, with the largest deviation right after the forcing was turned off. The transient terms, $a_5(\tau)$ and $a_6(\tau)$, while predicting correct trends, miss some details during the transient periods.

Many factors can contribute to the small differences between the model predictions and the experiment shown in Fig. 11. One possible reason is that while the system response was extracted at different initial times or phases during the natural to control transition, the flow was self-locked during the control to natural transition. Therefore, the model had sufficient information regarding how the system would transition from the natural to the controlled state, but due to the artificial self-phase-locking, only limited information was available about the transition from the controlled to the natural state. In order to

Table 1 Coefficients in system (10)

Linear terms	Quadratic terms	Cubic terms	Forcing
$c_1 = 557.7$, $l_{11} = -86.1$	$q_{111} = 1.8$, $q_{121} = -2.2$, $q_{131} = -2.3$, $q_{141} = -6.8$		$b_1 = -616.4$
$c_2 = 1016.9$, $l_{22} = -392.4$, $l_{23} = 263.9$	$q_{212} = 75.0$	$t_2 = -2.5$	$b_2 = -1016.9$
$c_3 = 41.0$, $l_{32} = -218.3$, $l_{33} = -7.6$	$q_{313} = 5.0$, $q_{314} = 3.9$	$t_3 = -0.2$	$b_3 = -41.0$
$c_4 = -628.9$, $l_{41} = 43.4$, $l_{44} = -113.5$	$q_{414} = 2.9$, $q_{424} = -9.8$, $q_{434} = 6.3$, $q_{444} = -7.3$		$b_4 = 222.8$
$c_5 = 182.4$, $l_{51} = -10.2$, $l_{55} = -39.1$, $l_{56} = 129.1$	$q_{515} = 3.9$, $q_{525} = 0.5$, $q_{535} = 0.7$	$t_5 = -0.2$	$b_5 = -279.7$
$c_6 = 271.6$, $l_{61} = -36.6$, $l_{62} = -42.0$, $l_{63} = 3.5$, $l_{65} = -117.4$, $l_{66} = -129.3$	$q_{626} = -0.4$, $q_{636} = -9.2$, $q_{646} = -25.5$, $q_{656} = 11.4$	$t_6 = 1.0$	$b_6 = -339.1$

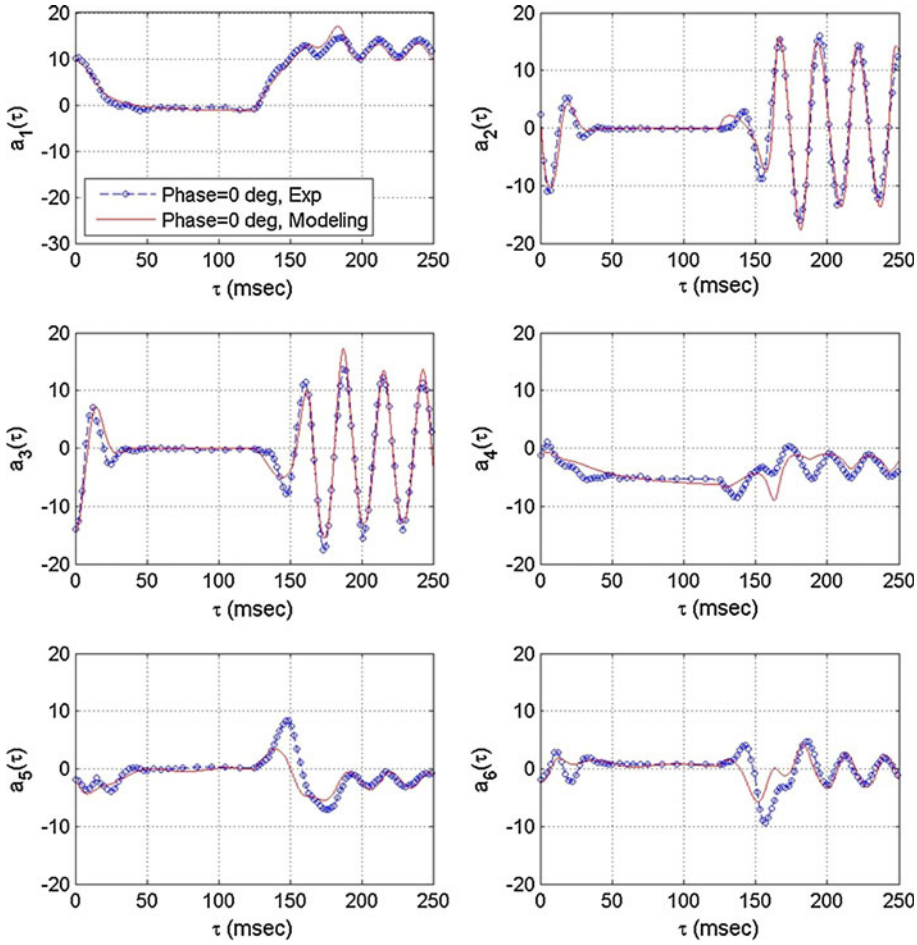

Fig. 11 Numerical solution of the system (7b) (*solid lines*) and experimental results (*dashed lines* with *symbols*) with the phase-locking value of 0 degrees. Actuation is turned on at 0 ms and turned off at 125 ms

Table 2 Coefficients in system (11)

Linear terms	Quadratic terms	Cubic terms
$c_1 = -78.3$, $l_{11} = -122.8$	$q_{111} = 5.3$, $q_{121} = -2.2$, $q_{131} = -4.3$, $q_{141} = -12.7$	
$l_{22} = -101.1$, $l_{23} = 269.7$	$q_{212} = 7.96$	$t_2 = -0.2$
$l_{32} = -239.3$, $l_{33} = -90.4$	$q_{313} = 8.37$	$t_3 = 0$
$c_4 = -877.0$, $l_{41} = 97.5$, $l_{44} = -150.3$	$q_{414} = 5.6$, $q_{424} = -17.6$, $q_{434} = 6.0$, $q_{444} = 3.8$	
$c_5 = 214.3$, $l_{54} = 67.3$, $l_{56} = 191.4$	$q_{515} = 16.6$, $q_{525} = -1.5$, $q_{535} = 7.6$, $q_{566} = 1.4$	$t_5 = -0.6$
$c_6 = -855$, $l_{62} = -68.7$, $l_{63} = -24.5$, $l_{64} = -185.6$, $l_{65} = -175.6$, $l_{66} = 23.6$	$q_{626} = 1.9$, $q_{636} = 4.7$, $q_{646} = 44.3$, $q_{656} = -1.4$	$t_6 = -1.0$

investigate this effect, a different model was designed to predict only the natural to controlled transition where well-defined initial conditions exist. To do that, the least-square estimate, Eq. (9), was integrated only between 0 and 50 ms. The resulting model is presented in Eq. (11) with numerical values of coefficients given in Table 2. Note that since the forcing was constant during this time interval, the forcing term was combined with constants, c_i, so the forcing term is not explicitly present in the model.

$$\frac{da_1(\tau)}{d\tau} = c_1 + l_{11}a_1 + q_{141}a_4a_1 + q_{111}a_1^2 + q_{121}a_2a_1 + q_{131}a_3a_1$$

$$\frac{da_2(\tau)}{d\tau} = \left[l_{22} + t_2\left(a_2^2 + a_3^2\right)\right]a_2 + l_{23}a_3 + q_{212}a_1a_2$$

$$\frac{da_3(\tau)}{d\tau} = l_{32}a_2 + \left[l_{33} + t_3\left(a_2^2 + a_3^2\right)\right]a_3 + q_{313}a_1a_3$$

$$\frac{da_4(\tau)}{d\tau} = c_4 + l_{41}a_1 + l_{44}a_4 + q_{444}a_4^2 + q_{414}a_1a_4 + q_{424}a_2a_4 + q_{434}a_3a_4$$

$$\frac{da_5(\tau)}{d\tau} = c_5 + l_{54}a_4 + t_5\left(a_5^2 + a_6^2\right)a_5 + l_{56}a_6 + q_{515}a_1a_5 + q_{525}a_2a_5 + q_{535}a_3a_5 + q_{566}a_6^2$$

$$\frac{da_6(\tau)}{d\tau} = c_6 + l_{62}a_2 + l_{63}a_3 + l_{64}a_4 + l_{65}a_5 + \left[l_{66} + t_6\left(a_5^2 + a_6^2\right)\right]a_6 + q_{626}a_2a_6 + q_{636}a_3a_6 + q_{646}a_4a_6 + q_{656}a_5a_6 \quad (11)$$

Experimental values of a-coefficients at $\tau = 0$ were used as initial conditions to numerically integrate the system (11). Results of the modeling for two different initial phases are shown in Fig. 12 along with corresponding experimental results. Now, the model predicts experimental results with better accuracy, with all essential features of the transition properly captured. The natural shedding for this model was 40.4 Hz, which, compared to the model (10), agrees better with the experimentally observed natural shedding frequency of 42 Hz. Also, unlike the model (10), the coefficients in the model (11) do not depend on the initial phase and the initial phase enters the model (11) only via initial conditions $a_i(\tau = 0, t_0)$.

6 Discussion

This paper has demonstrated a novel technique, temporal POD (TPOD), to extract the optimum set of eigenmodes and their temporal evolution from experimental data with the presence of active flow control. Retaining the time in TPOD modes allows one to extract important information

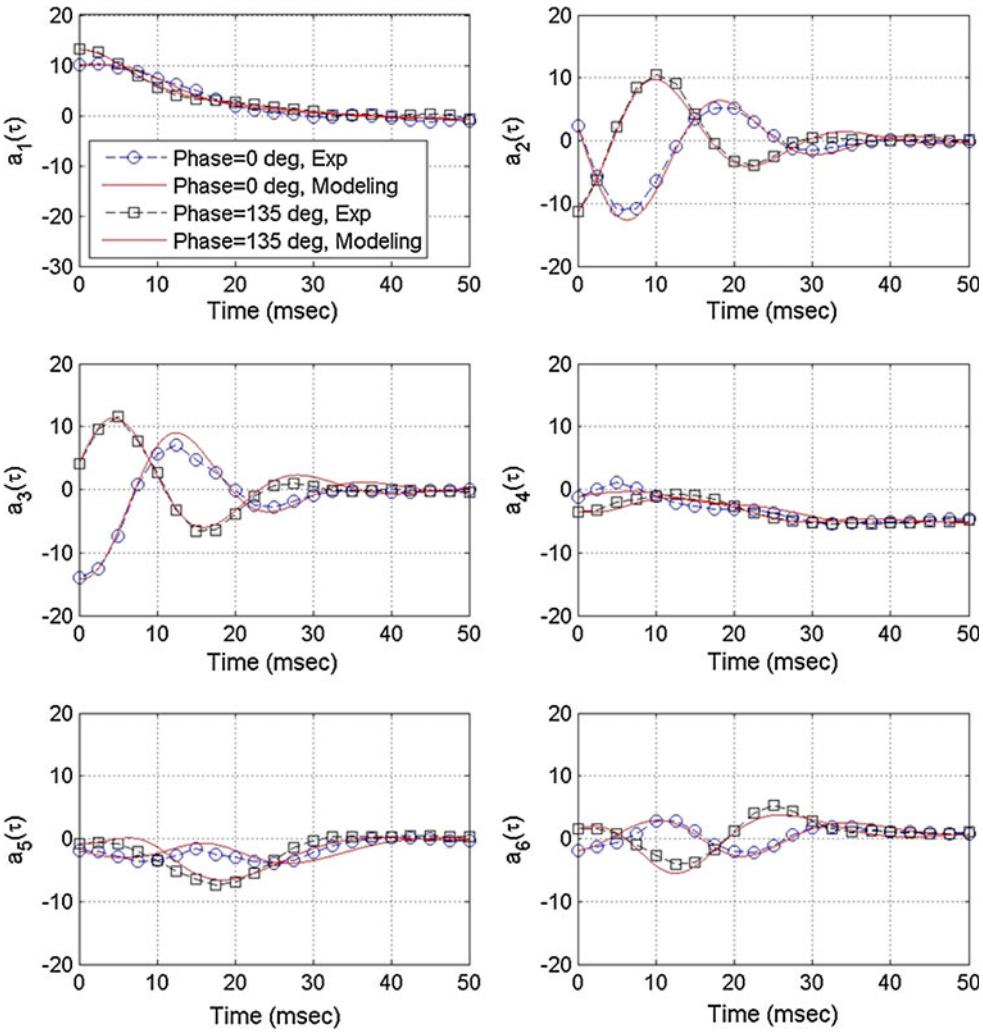

Fig. 12 Numerical solution of the system (11) (*solid lines*) and experimental results (*dashed lines* with *symbols*) for two representative phase-locked values of 0 and 135 degrees

about system trajectories from natural to controlled states and back in the optimum frame of reference. For illustrative purposes, the technique was applied to the wake flow downstream of a cylinder at subcritical Reynolds number. The extracted temporal coefficients were used to develop a nonlinear model containing linear, quadratic and cubic terms; a least-square analysis was used to analyze the importance of individual terms. The developed model showed excellent promise in capturing the dynamics of the natural, controlled and transient states of the flow, as well as hysteresis effects with the presence of the flow control. It is important to note that in order to build the model, no additional a priori knowledge about the flow dynamics was used.

In the case of cylinder flow control presented here, the natural state exhibits a simple limit cycle behavior. It is important to point out that the TPOD technique is readily adapted to more complex aperiodic flow fields. For example, in Gordeyev et al. (2011), TPOD was applied to the case of leading edge DBD plasma flow control of a NACA 0015 airfoil at a large post-stall attack angle of $\alpha = 18°$. High-speed PIV was used to capture the temporal evolution of the flow field as it cycled between natural and controlled states and back. The reader is referred to the above-cited reference for details regarding the experiment. In this case, TPOD was used to analyze small subsets or regions of the initial conditions, and different flow trajectories originating from these initial subsets were calculated and analyzed. In particular, after the TPOD modes were calculated, temporal coefficients, $a_i(\tau;t_0) = \int u(x,y;\tau,t_0)\,\phi_i(x,y;\tau)\mathrm{d}x\mathrm{d}y$, were computed for each flow realization. Figure 13 shows all temporal coefficients for the first two TPOD modes at $\tau = 0$ ms, just before the flow control was activated. Unlike the flow around the cylinder, where initial points were contained on a simple limiting cycle (see Fig. 8), all initial points for the airfoil flow in the natural state occupy a more complex region.

The temporal evolution of the coefficients for the first two modes for all 250 flow trajectories is plotted in Fig. 14a, revealing a complex set of different trajectories from the natural to the controlled state. To illustrate the ability of the TPOD approach to extract conditional-averaged events, two distinct small subsets or regions of the initial conditions were arbitrarily selected. The first group, labeled by black circles in the far upper left corner in Fig. 13, represents a statistically rare event in the flow. The second group of initial conditions is labeled by red circles in Fig. 13 and represents a more typical transient event. Once the initial conditions were selected, the temporal evolutions of the TPOD coefficients for the selected subsets were calculated, along with the subset-ensemble-averaged

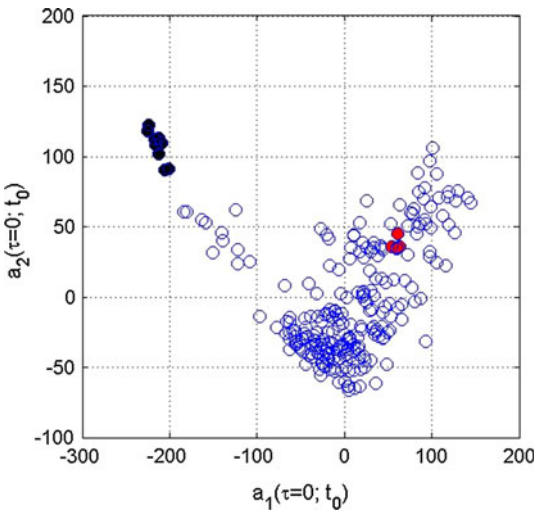

Fig. 13 Values of temporal coefficients of the first and the second TPOD modes at $\tau = 0$ for flow over NACA 0015 airfoil. Two selected groups of initial conditions are labeled by *black* and *red circles*. From Gordeyev et al. (2011)

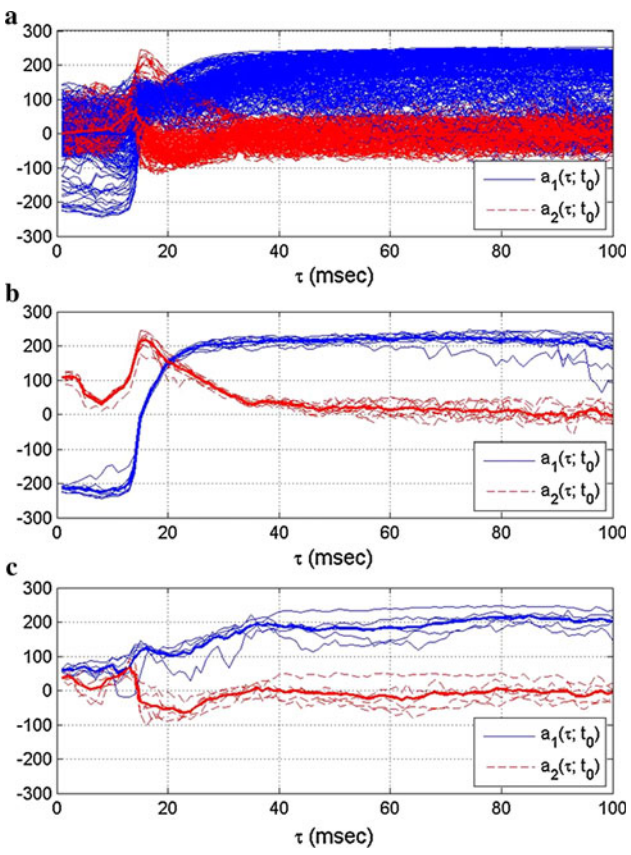

Fig. 14 Temporal evolution of the first two TPOD modes for **a** all trajectories, and trajectories originated from the two groups, labeled by **b** *black* and **c** *red circles* in Fig. 13. Corresponding conditionally averaged trajectories for both TPOD modes are plotted as *thicker lines* in plots B and C. From Gordeyev et al. (2011)

trajectories for both groups. The results for the first group are shown in Fig. 14b. All trajectories exhibited some small stochastic variation around the ensemble-averaged trajectory. The first TPOD mode remained at a constant value of -200 for the first 15 ms, after which it quickly went to a value of approximately 200 between 15 and 30 ms and subsequently remained essentially constant at $\tau > 30$ ms. The second TPOD mode was essentially non-zero during the first 50 ms before leveling off at a zero-value. Trajectories in the second group shown in Fig. 14c exhibit a larger spread from the conditionally averaged trajectory. Although the final trajectory values are the same, the transient process was slower for this group of trajectories, with both modes leveling off at approximately $\tau = 70$ ms after the flow control was activated.

Using conditionally averaged trajectories of the first two TPOD modes, corresponding instantaneous velocity fields for conditional-averaged trajectories for both groups of initial conditions were re-created. Inspection of the reconstructed velocity field for the first group, the statistically rare event denoted by black circles in Fig. 13, revealed that the flow was already partially attached before the flow control was activated, and therefore, it quickly became fully attached over the suction side of the airfoil when the flow control was activated. In contrast, results of the velocity reconstruction for the trajectories in the second group identified as the more common event and denoted by red circles in Fig. 13 showed that the flow was fully separated before the flow control was activated, and as a consequence, it took the flow a longer period of 40 ms to go to the control state.

Thus, for both examples in this paper, the TPOD method is shown to provide the ability to conditionally examine families of flow trajectories between natural and controlled states for user-selected initial conditions, t_0, and to successfully build relatively simple low-dimensional models which correctly reflect the transient behavior of the system for different initial flow states. This knowledge is very useful in order to understand the physical mechanisms of flow control in complex flows where there may be very little a priori knowledge of the system behavior. Unlike traditional conditional-sampling experiments, where the conditional event is typically defined and fixed before the experiment, the knowledge of flow trajectories given by the TPOD technique allows one to redefine the conditional event and analyze the data without the need to redo the experiment. This feature allows one to efficiently and quickly study the flow response to the actuation for different initial flow states. Also, for traditional conditional sampling, where the system evolution is studied *after* the conditional event, the knowledge of TPOD-based flow trajectories in space and time allows one to investigate the system evolution *before and after* the conditional event. This is extremely useful for flow control applications if, for example, a conditional event is defined after the flow control is applied and trajectories can be traced back in time to find out which subset of the initial times would lead to the desired event in the future.

Acknowledgments The authors would like to acknowledge the financial support of NASA through Cooperative Agreement NNX07AO09A. The time-resolved PIV system used in the airfoil study was acquired under DURIP award W911NF-10-1-0164 administered through the Army Research Office. The authors would also like to acknowledge the important contributions of Lee Neuharth and Michael Wicks in the data acquisition.

References

Aubry N, Holmes P, Lumley JL, Stone E (1988) The dynamics of coherent structures in the wall region of the turbulent shear layer. J Fluid Mech 192:115–175

Ausseur M, Pinier JT (2005) Toward closed-loop feedback control of the flow over NACA-4412 Airfoil. In: 43rd AIAA aerospace sciences meeting and exhibit, Jan 2005, AIAA-2005-343

Berkooz G, Holmes P, Lumley JL (1993) The proper orthogonal decomposition in the analysis of turbulent flows. Ann Rev Fluid Mech 25:539–575

Camphouse RC, Myatt JH, Schmit RF, Glauser MN, Ausseur JM, Andino MY, Wallace RD (2008) A snapshot decomposition method for reduced order modeling and boundary feedback control. In: 4th Flow control conference, 2008, AIAA-2008-4195, Seattle, Washington

Corke TC, Post ML, Orlov DM (2009) Single dielectic barrier discharge plasma enhanced aerodynamics: physics, modeling and applications. Exp Fluids 46(1):1–26

Gordeyev S, Neuharth L, Thomas FO, Wicks M (2011) Further experiments on temporal proper orthogonal decomposition for closed-loop flow control. In: 41st AIAA fluid dynamics conference, 27–30 June 2011, Honolulu, Hawaii, AIAA paper 2011-3717

Holmes P, Lumley JL, Berkooz G (1996) Turbulence, coherent structures, dynamical systems and symmetry. Cambridge University Press, Cambridge

Juang JN, Pappa RS (1985) An eigensystem realization algorithm for modal parameter identication and model reduction. J Guid Contr Dyn 8(5):620–627

Kozlov AV, Thomas FO (2011) Bluff body flow control via two types of dielectric barrier discharge plasma actuation. AIAA J 49(9): 1919–1931

Luchtenburg DM, Günther B, Noack BR, King R, Tadmor G (2009) A generalized mean-field model of the natural and high-frequency actuated flow around a high-lift configuration. J Fluid Mech 623:283–316

Lumley J (1970) Stochastic tools in turbulence. Academic, New York

Ma Z, Ahuja S, Rowley CW (2010) Reduced order models for control of fluids using the eigensystem realization algorithm. Theoret Comput Fluid Dyn (online)

Moreau E (2007) Airflow control by non-thermal plasma actuators. J Phys D Appl Phys 40(3):605–636

Rowley CW (2005) Model reduction for fluids using balanced proper orthogonal decomposition. Int J Bifurcation Chaos 15(3):997–1013

Siegel SG, Seidel J, Fagley C, Luchtenburg DM, Cohen K, McLaughlin T (2008a) Low-dimensional modeling of a transient cylinder wake using double proper orthogonal decomposition. J Fluid Mech 610:1–42

Siegel SG, Cohen K, Seidel J, Aradag S, McLaughlin T (2008) Low dimensional model development using double proper orthogonal decomposition and system identification. In: 4th Flow control conference, June, 2008, AIAA-2008-4193

Sirovich L (1987) Turbulence and the dynamics of coherent structures, parts I–III. Q Appl Math 10(3):561–582

Tadmor G, Noack BR, Morzynski M, Siegel S (2004) Low-dimensional models for flow control. Part II. Control and dynamic estimation. In: 2nd flow control conference, June 2004, AIAA-2004-2409

Thomas FO, Kozlov A, Corke TC (2008) Plasma actuators for cylinder flow control and noise reduction. AIAA J 46(8):1921–1931

Thomas FO, Corke TC, Iqbal M, Kozlov A, Schatzman D (2009) Optimization of SDBD plasma actuators for active aerodynamic flow control. AIAA J 47(9):2169–2178

Ukeiley LS, Cordier L, Manceau R, Delville J, Glauser MN, Bonnet JP (2001) Examination of large-scale structures in a turbulent plane mixing layer. Part 2. Dynamical systems model. J Fluid Mech 441:67–108

Zdravkovich MM (1997) Flow around circular cylinders. Vol. 1: fundamentals. Oxford University Press, Oxford (Chap. 6)